

Open-PMC-18M: A High-Fidelity Large Scale Medical Dataset for Multimodal Representation Learning

Negin Baghbanzadeh^{1,2,*}

Mohammed Saidul Islam^{1,2,*}

Sajad Ashkezari^{1,3,*}

Elham Dolatabadi^{1,2}

Arash Afkanpour¹

¹Vector Institute ²York University ³University of Waterloo *Equal contribution

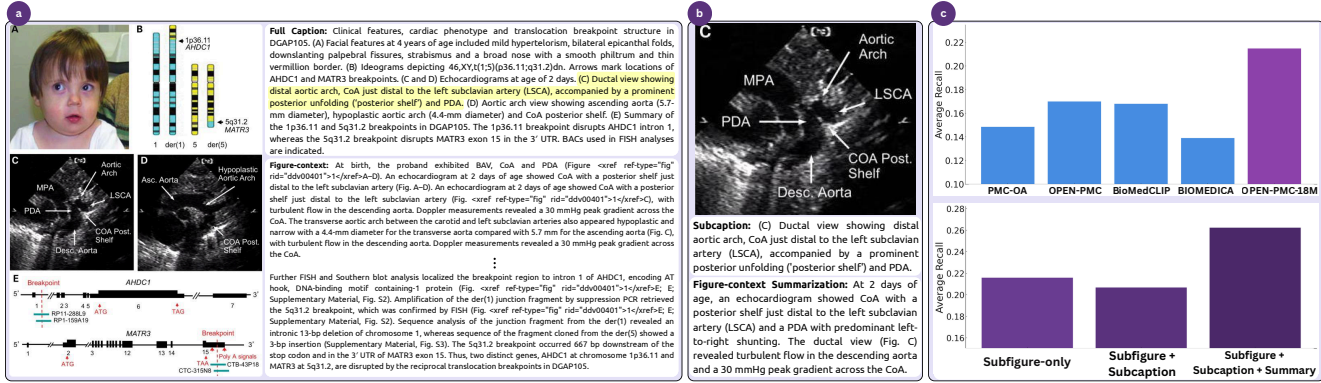


Figure 1. (a) Compound figure, and corresponding full caption (subcaption for subfigure ‘C’ is highlighted) and in-text reference related to the figure from BIOMEDICA dataset; (b) Extracted subfigure image from OPEN-PMC-18M, and corresponding extracted subcaption and summary of in-text reference; (c) Average retrieval performance: our model vs. other models (top), and Retrieval results on MIMIC-CXR of model versions trained in different settings: subfigure only vs. subfigure + subcaption vs. subfigure + subcaption + summary (bottom). The compound image in (a) is originally from [25].

Abstract

In biomedical vision-language modeling, datasets are typically mined from scientific literature, pairing compound figures with captions that are short, context-dependent, and often partially informative. Prior work on subfigure extraction has been limited in both dataset size and generalizability. In addition, no existing effort has incorporated rich medical context in image-text pairs. We revisit data curation as a foundational component of effective biomedical representation learning. Our data curation process integrates transformer-based subfigure detection, subcaption extraction, and contextual text enrichment derived from inline references. Our subfigure extraction model, trained on a corpus of 500,000 compound figures, achieves state-of-the-art performance on real and synthetic benchmarks. Using this process, we curate and release **OPEN-PMC-18M**, a large-scale high-fidelity biomedical dataset comprising 18 mil-

lion image-text pairs, spanning radiology, microscopy, and visible light photography. We train vision-language models on our dataset and perform extensive evaluation on 6 retrieval and 19 zero-shot classification tasks across three major modalities. The models trained on our dataset set a new state-of-the-art results in medical representation learning. We release our dataset, models, and code to support reproducible benchmarks and further study into biomedical vision-language modeling and representation learning.

1. Introduction

The rapid progress of general-domain vision-language models (VLMs) [8, 13, 27] has inspired growing efforts to build large-scale multimodal datasets for scientific and biomedical representation learning [1, 17, 20, 24, 43]. These models learn unified image-text representations that

enable cross-modal retrieval and zero-shot classification, and can be further integrated with generative decoders to support downstream medical reasoning and report synthesis tasks [16, 28].

A common approach to learn representations is via a contrastive pretraining objective, which aligns visual and textual embeddings in a shared semantic space [27, 35]. While broadly applicable, its effectiveness depends on the fidelity of the paired supervision [37]. In natural web data, such as those used for CLIP [27] and subsequent models [22, 40], the paired text (captions, metadata, or surrounding paragraphs) is typically descriptive and diverse, providing rich linguistic grounding for visual concepts [6, 37]. As later revealed by MetaCLIP [37], much of CLIP’s success stems largely from meticulous data curation. This ensures that each image-text pair contributes semantically informative signals to the shared space.

In the biomedical domain, however, the paired supervision is constructed differently. Most medical VLMs are trained on datasets mined from scientific literature, such as PubMed Central (PMC)¹ (e.g, PMC-15M [43] and BIOMEDICA [20]), in which figures and captions are extracted to form image-text pairs (see Figure 1(a)). This introduces two fundamental challenges. First, biomedical figures are often *compound* or multi-panel, combining heterogeneous content, including radiology scans, microscopy images, plots, and annotations. Second, the corresponding captions are frequently symbolic, abbreviated, or context-dependent, relying heavily on in-text references rather than self-contained descriptions. Pairing a compound image with a partially informative caption produces a data point that, when used for representation learning, leads to suboptimal representations. Yet, most existing datasets are formed in this manner.

These mismatches produce coarse image-text alignments during pretraining, introducing systemic errors into representation learning and encouraging models to fit to superficial or repetitive textual anchors rather than learning precise biomedical semantics. Over time, this weakens cross-modal correspondences and limits transfer to downstream tasks that demand fine-grained understanding. Thus, biomedical data amplify the lessons of MetaCLIP: high-fidelity VLMs require deliberate reconstruction of meaningful image-text pairs, not raw extraction of figures and captions.

One might argue that at sufficient data scale and model complexity, such error will vanish [32]. However, scientific corpora such as PubMed Central, remain orders of magnitude smaller than open-web sources. Moreover, even in the natural domain, gains in zero-shot performance have been traced to curation and distributional balancing rather than sheer scale or architectural novelty [29, 30, 37]. This suggests that representation quality in medical VLMs is

constrained more by data structure and alignment than by dataset size or model capacity.

To our knowledge, no prior work has jointly incorporated both subfigure extraction and contextual text summarization into a unified biomedical vision-language dataset, nor evaluated their impact on representation learning. A few prior works tackled subfigure extraction but at limited accuracy and scale [1, 17, 24]; contextual enrichment has been largely unaddressed.

This raises an important gap in the field: *how does subfigure extraction and contextual text summarization affect the quality of learned representations in the medical domain, particularly given the known sensitivity of contrastive objectives to dataset alignment and scale during pretraining?*

We introduce OPEN-PMC-18M, the first large-scale and carefully curated dataset comprising 18 million subfigure-text pairs, where each text entry consists of an associated *subcaption*, extracted from the original caption, and a summary of inline context that explicitly references the subfigure (Figure 1(b)). Starting from the BIOMEDICA corpus [20], which is extracted from PubMed Central, we apply metadata-level filtering using label annotations and a ResNet-based classifier to remove non-medical or schematic content. For subfigure extraction, we train a high-performance detector on a dataset of 500,000 programmatically generated compound figures. For subcaption extraction we utilized Qwen2.5-VL-32B-Instruct VLM [2] and text summarization we used Qwen2.5-14B-Instruct [26].

We train vision and text encoders using contrastive loss on OPEN-PMC-18M and evaluate the encoders on an extensive suite of downstream tasks, including cross-modal retrieval and zero-shot classification tasks across three major medical modalities: radiology, microscopy, and visible light photography (VLP). We release our dataset, models, and code² to support reproducible benchmarks and further study into biomedical VLM and representation learning. Our contributions are as follows:

- We curate and release OPEN-PMC-18M, a large-scale high-fidelity biomedical image-text dataset with 18 million image-text pairs, each consists of a subfigure paired with the corresponding subcaption and image-context summary.
- We propose a scalable and accurate subfigure extraction pipeline based on transformer-based object detection, trained on 500,000 compound figures, achieving state-of-the-art performance on ImageCLEF 2016 [7, 15] and synthetic evaluation sets.
- We perform a comprehensive evaluation of VLMs trained on OPEN-PMC-18M, demonstrating improved performance in retrieval (Figure 1 (c) (top)), classification, and robustness across multiple medical benchmarks in radiol-

¹<https://pmc.ncbi.nlm.nih.gov/>

²<https://github.com/vectorInstitute/pmc-data-extraction>

ogy, microscopy, and visible light photography.

2. OPEN-PMC-18M Composition and Curation Process

Our dataset curation pipeline (Figure 2 (a)) contain three key stages: (i) Initial Figure Collection and Filtering, (ii) Vision-Based Subfigure Extraction, and (iii) Textual Enrichment via subcaption extraction and summary generation. Below we describe each stage in detail.

2.1. Initial Figure Collection and Filtering

To curate our dataset we start with the BIOMEDICA dataset [20], which has been extracted from articles in the PubMed Central Open Access Subset. BIOMEDICA contains approximately 24 million image-caption pairs along with in-text figure references, often spanning multiple paragraphs. BIOMEDICA obtains image modalities by extracting visual features of each image using a DINO-v2 model [4], followed by clustering of images with PCA and K-means. Clusters are then annotated by experts which provide 12 global modality labels (e.g., clinical image, microscopy, immunoassays, chemical structures) and 170 local labels (e.g., magnetic resonance imaging, X-ray radiography, computed tomography, etc.)

To improve dataset quality, we apply a filtering step using the provided labels and retain only those pairs primarily categorized as clinical imaging, microscopy, immunoassays, or chemical structure. This yields a dataset of 6 million pairs, which we refer to as PMC-6M in this paper.

2.2. Vision-Based Subfigure Extraction

To extract subfigures from biomedical compound figures with high accuracy at scale, we trained a transformer-based object detection model based on the *Dynamic Anchor Box DEtection TRansformer* (DAB-DETR) architecture [18]. Prior work of Lin et al. [17] trained a DETR model for the same purpose on MedICaT [31] with only 2,069 manually annotated compound figures. In contrast, we trained our model on a large-scale synthetic dataset of 500,000 compound figures, which we explain below. This dataset is the first of its kind in the biomedical domain. We use DAB-DETR as it improves upon the original DETR model by learning dynamic anchors as queries, resulting in improved localization and faster convergence [18].

Synthetic Data Formation. To train a subfigure extraction model, we generate a synthetic dataset by reversing the subfigure extraction process: rather than decomposing existing compound figures, we programmatically construct new ones by composing multiple single-panel biomedical images into compound layouts. The key advantage of this approach is the availability of ground-truth bounding boxes

for each subfigure. To create diverse layouts, our generation pipeline samples a layout template that specifies the spatial arrangement of subfigures from a large number of configurations. Each layout is defined by a set of configurable parameters, including:

- **Grid Size:** Specifies a standard $m \times n$ grid or a custom arrangement for panel placement.
- **Margins:** Random horizontal and vertical spacing between panels to simulate variability in published figure layouts.
- **Labeling Scheme:** Determines how panels are annotated (e.g., using numerical, alphabetical, or compound labels like “1a” or “a-1”), and whether labels appear inside or outside panel boundaries.
- **Aspect Ratio:** Specifies a fixed width-to-height ratio applied uniformly to all subfigures.

Subfigures are sampled from single-panel biomedical images spanning diverse modalities (also sourced from the metadata) such as radiology, microscopy, and VLP, which we will describe below. Composite figures may contain panels from the same modality or a heterogeneous mix, providing semantic diversity and mimicking real-world figure complexity. Figure 2(b)) illustrates the full synthetic data pipeline.

Image Decomposition Model Training and Evaluation.

We train a DAB-DETR model on the 500,000 compound figures and validate its performance on a similarly created holdout set of 20,000 images. Source subfigures are drawn from well-known benchmark datasets such as ROCO [24], SICAP [44], HAM10000 [33], PathMNIST and RetinaMNIST from MedMNIST [38, 39], PAD-UFES-20 [23], and PlotQA [21] as listed in Table 1. To ensure balanced representation, each modality-specific dataset contributes approximately 16.7% of the total examples, with the remaining 16.7% comprising mixed-modality compound figures. This configuration promotes both visual diversity and generalization across biomedical imaging types. Training is performed over 40 epochs using a batch size of 64 and an initial learning rate of 10^{-5} .

We evaluate performance on both our synthetic validation set and the ImageCLEF 2016 compound figure separation benchmark [7, 15]. For comparison, we benchmark against a DETR model trained on MedICaT [31] and the Qwen2.5-VL-32B-Instruct [2] multimodal model, which we adapt for zero-shot subfigure detection by prompting bounding-box prediction on compound figures. As shown in Table 2, our DAB-DETR substantially outperforms both baselines. Figure 2(c) presents qualitative examples from the ImageCLEF 2016 dataset, and additional results from a subset of PMC-6M are shown in Figure 9 in Appendix §E. Together, these examples demonstrate our model’s ability to accurately detect distinct subfigures across heterogeneity.

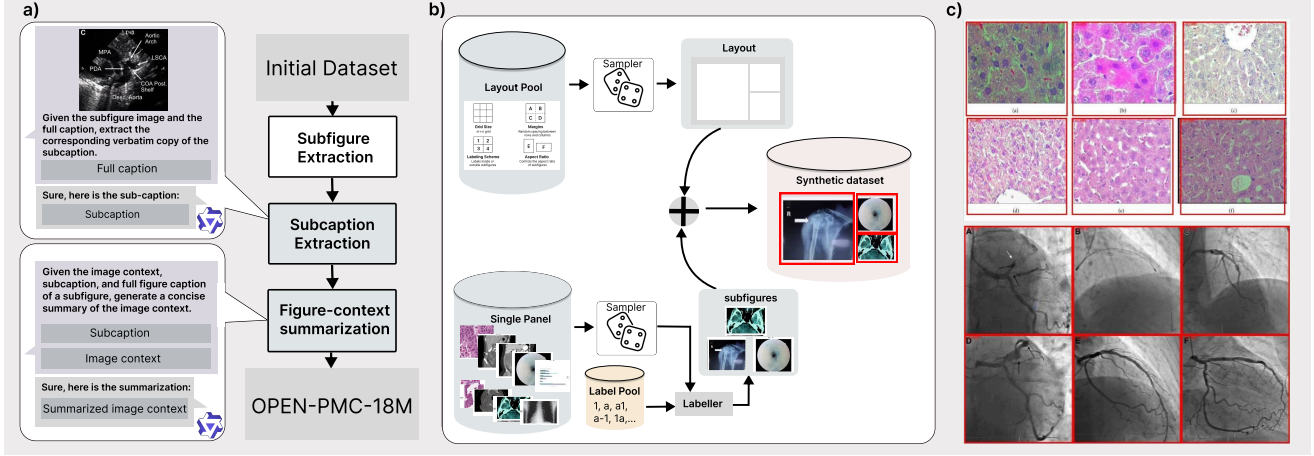


Figure 2. (a) Overview of the OPEN-PMC-18M construction process comprising of the following key stages: (b) Subfigure Extraction pipeline for creating synthetic compound figures that are used to train the DAB-DETR model. (c) Example subfigures extracted using the DAB-DETR model from ImageCLEF dataset.

neous layouts and content types, in contrast to the inconsistent or missing predictions observed with Qwen2.5-VL-32B-Instruct (Figure 10 in Appendix).

Table 1. Single panel datasets used to construct the synthetic compound figure corpus, categorized by modality and split. The training and validation sets are composed of single modality images that serve as source panels for synthetic figure generation. * indicates the held-out test portion of ROCO, and + denotes the official validation split.

Modality	Train (Examples)	Validation (Examples)
Radiology	ROCO (65422)	ROCO* (8176)
Histopathology	SICAP (18783)	PathMNIST (10004)
Dermatology	HAM10000 (10015)	PAD-UFES-20 (2298)
Retina	RetinaMNIST (1080)	RetinaMNIST ⁺ (120)
Plots	PlotQA (60000)	PlotQA ⁺ (10000)

Table 2. Comparison of subfigure detection performance on two datasets using mAP and F1 metrics. * Previous SOTA (MediCaT-trained DETR), ⁺ Qwen2.5-VL-32B-Instruct, and ^o our DAB-DETR model.

Model	Synthetic Validation		ImageCLEF 2016	
	mAP (%)	F1 (%)	mAP (%)	F1 (%)
SOTA*	33.22	73.18	28.20	64.85
Qwen ⁺	40.31	79.01	30.12	68.12
Ours ^o	98.58	99.96	36.88	73.55

2.3. Text Enrichment

To enrich the dataset with contextual information relevant to each subfigure, we employed two key methods: (a) We

extracted the corresponding subcaption from the full caption to improve image-text alignment, and (b) We identified in-text reference paragraphs from the metadata and summarized them to further enrich the semantic content related to each subfigure.

Subcaption Extraction The majority of captions in the dataset consist of multiple subcaptions, generally distinguished by delimiters such as (a), (b), or (A–F). Given that the total number of subfigures is approximately 18 million, manual extraction of all subcaptions is not feasible. To address this, we adopted an automated extraction method using a state-of-the-art open-source VLM, i.e., Qwen2.5-VL-32B-Instruct [2]. For each sample, we designed a prompt comprising the full caption, a subfigure image, and additional instructions (Figure 7 in the Appendix) for subcaption extraction.

To ensure determinism and prevent hallucinations or inaccuracies, the model was explicitly instructed to extract a verbatim copy of the subcaption directly from the full caption, without adding any additional text or explanation. In cases where a subcaption could not be found, the model was instructed to extract the verbatim copy of the full caption instead. Overall, we found that 13.28% of subcaptions in the dataset are exact copies of their full captions. To evaluate the quality of our automated extraction method, we manually reviewed a random sample of 1,000 instances and observed that in 94% of cases the subcaptions were correctly extracted. The erroneous cases were primarily due to missing subcaptions, indicating that the model performs reliably for large-scale automated subcaption extraction.

Inference was conducted on 32×A100 GPUs (4 nodes), requiring roughly 13,474 GPU-hours (17.5 wall-clock

days), with an average per-instance inference time of 3 seconds.

In-text Reference Summarization Since the compound figures of OPEN-PMC-18M were collected from the BIOMEDICA dataset [20], we used the dataset’s accompanying image metadata, such as *image context* which are in-line text references associated with each compound figure. However, these references frequently extend across multiple paragraphs. In many cases, important contextual details appear outside the sentences that directly correspond to a subfigure, making it difficult to determine which pieces are related to a particular subfigure. To mitigate these issues, we employed the Qwen2.5-14B-Instruct [26] model to generate concise, context-aware summaries that distill the most relevant information while retaining essential details for each subfigure. For this task, we used this model instead of Qwen2.5-VL-32B-Instruct because the summary generation task involves only textual input and the 14B model is a text-only model optimized for instruction following and long-context generation [26], making it a more suitable and computationally efficient option.³ For each sample, we designed a prompt comprising the full caption, a subcaption related to a subfigure image, the image context, and additional instructions. We provide the full prompt in Figure 8 in the Appendix (§D).

2.4. Final Refinement

Decomposing the compound images of PMC-6M using our DAB-DETR model yields an initial dataset of approximately 32 million. To ensure the final dataset contains only biomedical images, we apply an additional filtration using global modality metadata fields to only keep subfigures whose original compound figure was labeled as either Clinical Image or Microscopy, which yields a dataset of 26 million pairs. Subsequently, we employ a ResNet-101 model [17] to assess each image and infer its medical relevance. This filtering process further reduces the dataset to 18 million high-quality image-caption pairs.

2.5. Dataset Statistics

OPEN-PMC-18M contains 12,997,862 microscopy images (73%), 3,244,121 radiology images (18%), 1,421,804 visible light photography images (8%), and 204,212 other clinical imaging samples (1%). Full caption lengths are highly variable, with most captions between 50 and 200 tokens, an average length of 165.8 tokens, and a maximum length of 7352; about 19.48% of captions exceed 256 tokens. Subcaption lengths are relatively short and consistent across the dataset. The average subcaption contains 30 tokens with

³The 14B model takes on average 0.64s per instance as opposed to 3s for Qwen2.5-VL-32B-Instruct.

majority (82.91%) containing less than 50 tokens. An additional 16.59% of subcaptions contain between 50-150 tokens, and only 0.50% exceed 150 tokens. Figure-context summaries are longer and demonstrate greater variability compared to subcaptions. The average summary length is 54 tokens. Less than half of summaries (46.21%) contain fewer than 50 tokens, whereas 53.68% are within the 50–150 token range. Only 0.11% of summaries exceed 150 tokens. We limit the summaries to be less or equal to 256 tokens by limiting the maximum token generation to 256 tokens during model inference. In terms of figure structure, most figures contain between one and three subfigures, though some include up to 20. Detailed visualizations are provided in Figure 4 in the §A of the Appendix.

3. Experiments

3.1. Encoder Pretraining

We train separate image and text encoders by aligning their representations using a vanilla contrastive loss [35]. See §B.1 for more details.

3.2. Evaluation Setup

To systematically assess the impact of dataset scale and curation quality, we perform evaluations along both dimensions. We train all models under a unified architecture and training protocol to ensure controlled evaluation. For models without accessible training data, we instead use publicly released checkpoints obtained from HuggingFace. For the text encoder, we use PubMedBERT [10], and for the vision encoder, we adopt a ViT-B/16 transformer [5] pretrained on ImageNet. Encoders are trained for 60 epochs with a batch size of 2,048, and the best performing checkpoints are selected according to cross-modal retrieval performance on a held-out validation subset of 50,000 randomly sampled pairs. Details of the validation procedure and selection criteria are provided in the Appendix (§B.3). Image–text pairs used for training consist of subfigures, the extracted subcaptions, and summarized inline text. Training was performed on 8×A100 GPUs and completed in five days. We conducted our experiments using the open-source *mmlearn* multimodal learning framework.⁴

To establish a baseline, we train VLM encoders on the PMC-6M dataset, where each image-text pair consists of a compound image in its original form (Section 2.1). We also include publicly available checkpoints from other models trained on PMC-15M [43] and BIOMEDICA [20]. For BIOMEDICA, we use the checkpoint referred to as BMC-CLIP_{CF} in Lozano et al. [20], which is trained on a filtered subset of the full dataset, achieving state-of-the-art performance at the time of publishing BIOMEDICA [20].

⁴<https://github.com/VectorInstitute/mmlearn/tree/main>

For PMC-15M, we use the checkpoint trained on 15 million image-caption pairs, referred to as BioMedCLIP in Zhang et al. [43]. All external checkpoints were obtained from their official HuggingFace repositories and are evaluated using our standard downstream protocols.

To further ensure consistency, we independently reproduce the PMC-OA dataset [17] and train encoders using the same architecture and hyperparameters as those used for OPEN-PMC-18M and PMC-6M. Throughout the paper, all encoder variants are referenced by the name of the dataset on which they are trained, to facilitate transparent comparison. All the details of pretraining and hyperparameters are listed in the §B in the Appendix.

3.3. Downstream Tasks

The performance of the encoders is evaluated on several datasets across two primary tasks: retrieval and zero-shot classification. For the retrieval task, we measure both image-to-text and text-to-image retrieval across three datasets representative of distinct medical imaging modalities: Quilt [12] (microscopy), MIMIC-CXR [14] (radiology), and DeepEyeNet [11] (VLP). To evaluate robustness in retrieval, we follow established protocols from [19] by applying a suite of low-level visual perturbations, including brightness adjustment, spatial shift, rotation, horizontal flip, and zoom, directly to the test images. To assess the statistical significance of robustness differences, we employ the Wilcoxon signed-rank test, a non-parametric method for paired comparisons [36]. We consider a p-value less than 0.01 as statistically significant. For classification, we evaluate models using both zero-shot and linear probing protocols across a diverse set of tasks: five in radiology, eight in microscopy, and six in VLP. We use our trained vision and text encoders to encode the image and question, respectively.

3.4. Cross-Modal Retrieval and Robustness

Table 3 and Figure 1 (c) (top) summarize the performance of various VLMs on cross-modal retrieval tasks across the three benchmark datasets. We report Recall@200 (other Recall metrics are included in the Appendix), with the final column showing the Average Recall (AR) aggregated across all tasks. Models trained on OPEN-PMC-18M (subfigures) and PMC-6M (compound figures) consistently outperform PMC-15M and BIOMEDICA across all tasks and retrieval directions. In particular, OPEN-PMC-18M sets a new state-of-the-art with an AR of 21.64, showing a 27% relative improvement in average retrieval performance over the best previous model, OPEN-PMC.

Robustness, quantified as the ratio between retrieval performance under perturbations such as brightness adjustments, shifts, rotations, flips, and zoom distortions, and performance on the original data is presented in Figure 3.

Models trained on OPEN-PMC-18M consistently achieve higher robustness scores relative to baseline models, reflecting improved performance stability under input perturbations [42] in addition to superior retrieval performances. We observe statistically significant differences ($p < 0.01$) on Quilt and DeepEyeNet. These findings are particularly relevant to our focus on subfigure extraction and the potential for improved robustness in imaging modalities that exhibit high visual and semantic heterogeneity.

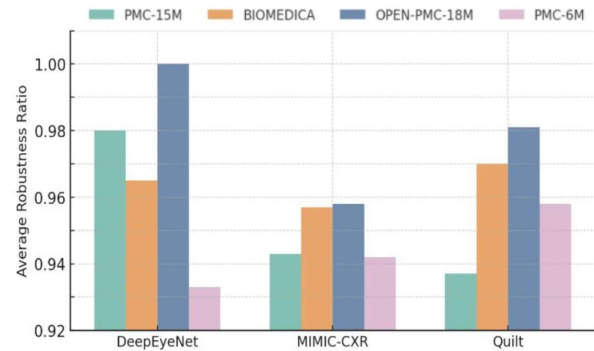


Figure 3. Robustness evaluation across retrieval benchmarks. Robustness is quantified as the ratio of performance under visual perturbations (brightness, shift, rotation, flip, zoom) to performance on the original test set. Higher values indicate greater stability to perturbations.

3.5. Zero-shot Classification

Model comparisons for zero-shot classification are presented in Table 4. For each modality, scores are averaged over multiple benchmark datasets (see Appendix Table 8 for details). Models trained on OPEN-PMC-18M, achieve the highest overall average, outperforming all existing biomedical VLMs. In particular, OPEN-PMC-18M shows large gains in microscopy and radiology tasks, and ranks second in radiology demonstrating better transferability relative to all other evaluated models. Across the full set of 19 classification tasks spanning radiology, microscopy, and VLP, OPEN-PMC-18M ranks first in 13 tasks and second in 1. A similar trend is observed in the linear probing results (Appendix Table 9), where OPEN-PMC-18M again achieves the highest average performance across modalities.

3.6. Representation Analysis

To further understand the effect of dataset scale and curation fidelity on learned representations, we visualize the embedding spaces of models trained on the PMC-6M (baseline) and OPEN-PMC-18M datasets. Both models share identical architectures and training hyperparameters, differing only in dataset composition, allowing a direct comparison.

Table 3. Retrieval performance (Recall@200) of all models trained on paired image-caption pairs in the medical domain. The last column, Average Recall (AR), aggregates the results across all tasks. Highest performance values are in bold, second-best are underlined. PMC-6M refers to a baseline model trained on a filtered subset of the BIOMEDICA dataset, using compound figures in their original form without subfigure decomposition. The BIOMEDICA model retrieved from HuggingFace is trained on a filtered subset of the full dataset, as described in their original paper.

Model	Image-to-Text			Text-to-Image			AR
	MIMIC-CXR	Quilt	DeepEyeNet	MIMIC-CXR	Quilt	DeepEyeNet	
PMC-OA	0.139	0.142	0.152	0.152	0.149	0.157	0.148
OPEN-PMC	0.17	0.166	<u>0.183</u>	0.189	0.162	0.147	0.17
BioMedCLIP	0.185	0.165	0.162	0.162	0.185	0.146	0.167
BIOMEDICA	0.076	0.169	0.155	0.093	0.195	0.145	0.139
PMC-6M	0.25	<u>0.203</u>	0.172	0.257	<u>0.22</u>	<u>0.170</u>	0.212
OPEN-PMC-18M	<u>0.215</u>	0.226	0.192	<u>0.210</u>	0.256	0.197	0.216

Table 4. Zero-shot classification average F1-scores across medical modalities.

Model	Radiology	VLP	Microscopy	Overall Avg
PMC-OA	30.95	29.79	42.62	34.45
OPEN-PMC	36.19	28.30	39.12	34.54
BioMedCLIP	28.62	21.17	43.35	31.04
BIOMEDICA	29.56	26.21	45.16	33.64
PMC-6M	30.28	<u>31.50</u>	<u>46.35</u>	<u>36.04</u>
OPEN-PMC-18M	<u>34.55</u>	32.10	55.35	39.77

ison of representation quality. We project the embedding spaces of three benchmark sets, each constructed by combining datasets used for retrieval and zero-shot classification across radiology, microscopy, and VLP, into two dimensions using t-SNE (Figure 6 in the Appendix). The radiology benchmark includes MIMIC-CXR and other related zero-shot classification tasks, totaling approximately 41,000 samples. The microscopy and VLP benchmarks contain approximately 20,000 and 6,000 samples, respectively. To quantify differences between the embedding distributions, we compute the Maximum Mean Discrepancy (MMD) [9] (more details in §C.1).

Visual inspection of the embeddings reveals distinct representational structures in the latent spaces of the models. Moreover, the MMD analysis confirms that the observed differences are statistically significant across all modalities. These results confirm that models trained on subfigure-level data with enriched textual context learn substantially different representations compared to models trained on compound figures and full captions without summaries.

4. Effects of Fine-Grained and Context-Enriched Language Supervision on Medical Representation Learning

We perform an ablation to examine the role of increasing textual fidelity. The results of this analysis are summarized

in Figure 1 (c) (bottom). To make the experiment computationally feasible, we restrict training to the radiology subset of OPEN-PMC-18M, which contains 3.2 million image–text pairs. All model variants use the same encoder architecture, optimization settings, and contrastive pretraining objective.

In the *Subfigure-only* variant, each subfigure is paired with its full caption. In *Subfigure + Subcaption*, the full caption is replaced by the extracted subcaption corresponding to that subfigure, providing finer-grained text alignment. Finally, in *Subfigure + Subcaption + Summary*, each subcaption is further augmented with a summary of its in-text context, capturing additional diagnostic or experimental details.

Results in Figure 1(c) (bottom) on MIMIC-CXR show that replacing full captions with subcaptions alone does not yield a performance gain, in fact, the reduced textual richness leads to a slight drop in average recall, highlighting that subcaptions, while more locally precise, may be too sparse to support robust alignment. However, when contextual summaries are added, performance increases substantially, indicating that the combination of panel-specific subcaptions and enriched contextual information provides the strongest supervision signal. Together, these findings suggest that high-quality biomedical representations rely not only on correcting local misalignment through subcaptions,

but also on restoring broader semantic and clinical grounding through contextual summaries.

5. Limitations and Challenges

Our findings suggest that in the context of vision-language representation learning, data quality and scale should be viewed as complementary axes in building effective and robust biomedical VLMs. Subfigure extraction, used here as a means to improve alignment quality, demonstrates clear benefits, particularly in visually heterogeneous domains such as microscopy and visible light photography, as shown in Figures 1 and 2. While our results highlight promising trends, additional analysis is required to fully assess generalization. Beyond representation quality, it is important to explore the integration of our encoders with large language model decoders for downstream tasks that involve generative reasoning over visual inputs, such as medical report generation and visual question answering, to establish a more grounded framework for multimodal clinical applications. Future work should also evaluate the factual consistency of these encoder, decoder systems relative to existing baselines, to determine whether well-curated, high-fidelity supervision improves not only discriminative performance but also the reliability of downstream generative tasks.

We recognize that scaling and curating large biomedical datasets brings challenges that extend beyond improving model performance. To support transparency and reproducibility, we release the dataset, data curation code, subfigure detection models, and training pipelines. However, interpretability remains an open challenge in VLMs and particularly in the biomedical domain. Although our models are not intended for clinical deployment, they could be fine-tuned or adapted for various clinical applications. However, without rigorous validation and careful consideration of clinical safety, such use poses serious risks.

Furthermore, our datasets, sourced from open-access repositories such as PubMed Central, may reflect underlying biases tied to specific institutions, imaging protocols, or publication norms. These factors can influence model behavior in subtle ways, limiting generalizability, especially when applied to underrepresented populations or distinct clinical settings.

6. Related Work

6.1. Biomedical Vision-Language Datasets

Most efforts to date have relied on mining figures and captions from the PMC Open Access subset.⁵ One of the earliest publicly available datasets is ROCO [24], which compiled around 80,000 radiology and 6,000 non-radiology images, enriched with metadata such as captions and key-

words. Later, Lin et al. [17] introduced PMC-OA, which includes 1.6 million image-text pairs. Their contribution emphasized automation, proposing a pipeline to streamline the pairing process and reduce human annotation. More recently, Zhang et al. [43] announced PMC-15M, a dataset of 15 million image-text pairs. The largest released dataset to date is BIOMEDICA [20], which comprises 24 million pairs and employs clustering, vision encoders, and expert labeling to assign modalities at global and local levels. While these efforts represent major progress at scale, recent work has emphasized that data quality is a critical factor in learning effective and generalizable medical representations [1]. Building on the premise of OPEN-PMC, our work takes a quality-first approach while also significantly scaling up the dataset.

6.2. Subfigure Extraction as Object Detection

Early approaches to compound figure separation relied on classical computer vision techniques, using heuristics based on whitespace, edge detection, or layout regularity. However, these methods often struggled to handle diverse panel styles and complex spatial arrangements. More recent work treats subfigure extraction as an object detection problem, leveraging deep learning models. For example, Tsutsui and Crandall [34] and Yao et al. [41] used YOLO for subfigure separation. Lin et al. [17] also uses an object detection model to extract subfigures in their pipeline. They train a DETR (DEtection TRansformer) model [3] on the MedLi-CaT dataset [31] containing 2069 annotated compound figures.

Data annotation for training an image decomposition model is challenging and time-consuming. Current annotated datasets for this purpose are small, which lead to models with suboptimal performance. To overcome this, synthetic datasets of compound figures have been proposed, where subfigures are programmatically composed to simulate real-world layouts. This allows training of object detection models without relying on large-scale human-annotated data [34, 41].

7. Conclusion

In this work, we addressed a fundamental limitation in current biomedical vision-language pretraining: the reliance on misaligned compound figures and weak medical context in image-text pairs. We introduced OPEN-PMC-18M, a large-scale, high-fidelity dataset constructed through accurate subfigure extraction and contextual text enrichment. Our systematic evaluations demonstrate that models trained on OPEN-PMC-18M achieve consistent gains across radiology, microscopy, and visible-light photography, outperforming existing PMC-derived datasets in retrieval, classification, and robustness. Beyond empirical improvements, our findings highlight a broader insight: effective biomed-

⁵<https://pmc.ncbi.nlm.nih.gov/tools/openftlist/>

ical representation learning depends more on precise data curation and alignment than on scale alone. We believe this dataset, and the accompanying analysis, provides a principled path toward multimodal models that are better aligned with the heterogeneous and context-dependent nature of real biomedical data.

References

- [1] Negin Baghbanzadeh, Adibvafa Fallahpour, Yasaman Parhizkar, Franklin Ogidi, Shuvendu Roy, Sajad Ashkezari, Vahid Reza Khazaie, Michael Colacci, Ali Etemad, Arash Afkanpour, et al. Advancing medical representation learning through high-quality data. *arXiv preprint arXiv:2503.14377*, 2025. [1](#), [2](#), [3](#), [8](#)
- [2] Shuai Bai, Kebin Chen, Xuejing Liu, Jialin Wang, Wenbin Ge, Sibo Song, Kai Dang, Peng Wang, Shijie Wang, Jun Tang, Humen Zhong, Yuanzhi Zhu, Mingkun Yang, Zhao-hai Li, Jianqiang Wan, Pengfei Wang, Wei Ding, Zheren Fu, Yiheng Xu, Jiabo Ye, Xi Zhang, Tianbao Xie, Zesen Cheng, Hang Zhang, Zhibo Yang, Haiyang Xu, and Junyang Lin. Qwen2.5-vl technical report. *arXiv preprint arXiv:2502.13923*, 2025. [2](#), [3](#), [4](#)
- [3] Nicolas Carion, Francisco Massa, Gabriel Synnaeve, Nicolas Usunier, Alexander Kirillov, and Sergey Zagoruyko. End-to-end object detection with transformers. In *European conference on computer vision*, pages 213–229. Springer, 2020. [8](#)
- [4] Mathilde Caron, Hugo Touvron, Ishan Misra, Hervé Jégou, Julien Mairal, Piotr Bojanowski, and Armand Joulin. Emerging properties in self-supervised vision transformers. In *Proceedings of the IEEE/CVF international conference on computer vision*, pages 9650–9660, 2021. [3](#)
- [5] Alexey Dosovitskiy, Lucas Beyer, Alexander Kolesnikov, Dirk Weissenborn, Xiaohua Zhai, Thomas Unterthiner, Mostafa Dehghani, Matthias Minderer, Georg Heigold, Sylvain Gelly, et al. An image is worth 16x16 words: Transformers for image recognition at scale. In *International Conference on Learning Representations*, 2020. [5](#)
- [6] Samir Yitzhak Gadre, Gabriel Ilharco, Alex Fang, Jonathan Hayase, Georgios Smyrnis, Thao Nguyen, Ryan Marten, Mitchell Wortsman, Dhruba Ghosh, Jieyu Zhang, Eyal Or-gad, Rahim Entezari, Giannis Daras, Sarah Pratt, Vivek Ramamujan, Yonatan Bitton, Kalyani Marathe, Stephen Muss-mann, Richard Vencu, Mehdi Cherti, Ranjay Krishna, Pang Wei W Koh, Olga Saukh, Alexander J Ratner, Shuran Song, Hannaneh Hajishirzi, Ali Farhadi, Romain Beaumont, Sewoong Oh, Alex Dimakis, Jenia Jitsev, Yair Carmon, Vaishaal Shankar, and Ludwig Schmidt. Datacomp: In search of the next generation of multimodal datasets. In *Advances in Neural Information Processing Systems*, pages 27092–27112. Curran Associates, Inc., 2023. [2](#)
- [7] Alba García Seco de Herrera, Roger Schaer, Stefano Bro-muri, and Henning Müller. Overview of the ImageCLEF 2016 medical task. In *Working Notes of CLEF 2016 (Cross Language Evaluation Forum)*, 2016. [2](#), [3](#)
- [8] Rohit Girdhar, Alaaeldin El-Nouby, Zhuang Liu, Mannat Singh, Kalyan Vasudev Alwala, Armand Joulin, and Ishan Misra. Imagebind: One embedding space to bind them all. In *Proceedings of the IEEE/CVF Conference on Computer Vision and Pattern Recognition*, pages 15180–15190, 2023. [1](#)
- [9] Arthur Gretton, Karsten M Borgwardt, Malte J Rasch, Bernhard Schölkopf, and Alexander Smola. A kernel two-sample test. *The Journal of Machine Learning Research*, 13(1):723–773, 2012. [7](#), [4](#)
- [10] Yu Gu, Robert Tinn, Hao Cheng, Michael Lucas, Naoto Usuyama, Xiaodong Liu, Tristan Naumann, Jianfeng Gao, and Hoifung Poon. Domain-specific language model pre-training for biomedical natural language processing, 2020. [5](#)
- [11] Jia-Hong Huang, C-H Huck Yang, Fangyu Liu, Meng Tian, Yi-Chieh Liu, Ting-Wei Wu, I Lin, Kang Wang, Hiromasa Morikawa, Hernghua Chang, et al. Deepopht: medical report generation for retinal images via deep models and visual explanation. In *Proceedings of the IEEE/CVF winter conference on applications of computer vision*, pages 2442–2452, 2021. [6](#)
- [12] Wisdom Ikezogwo, Saygin Seyfioglu, Fatemeh Ghezloo, Dylan Geva, Fatwir Sheikh Mohammed, Pavan Kumar Anand, Ranjay Krishna, and Linda Shapiro. Quilt-1m: One million image-text pairs for histopathology. *Advances in Neural Information Processing Systems*, 36, 2024. [6](#)
- [13] Chao Jia, Yinfai Yang, Ye Xia, Yi-Ting Chen, Zarana Parekh, Hieu Pham, Quoc Le, Yun-Hsuan Sung, Zhen Li, and Tom Duerig. Scaling up visual and vision-language representation learning with noisy text supervision. In *International conference on machine learning*, pages 4904–4916. PMLR, 2021. [1](#)
- [14] Alistair EW Johnson, Tom J Pollard, Seth J Berkowitz, Nathaniel R Greenbaum, Matthew P Lungren, Chih-ying Deng, Roger G Mark, and Steven Horng. Mimic-cxr, a de-identified publicly available database of chest radiographs with free-text reports. *Scientific data*, 6(1):317, 2019. [6](#)
- [15] Jayashree Kalpathy-Cramer, Alba García Seco de Herrera, Dina Demner-Fushman, Sameer Antani, Steven Bedrick, and Henning Müller. Evaluating performance of biomedical image retrieval systems– an overview of the medical image retrieval task at ImageCLEF 2004–2014. *Computerized Medical Imaging and Graphics*, 2014. [2](#), [3](#)
- [16] Chunyuan Li, Cliff Wong, Sheng Zhang, Naoto Usuyama, Haotian Liu, Jianwei Yang, Tristan Naumann, Hoifung Poon, and Jianfeng Gao. Llava-med: Training a large language-and-vision assistant for biomedicine in one day. *Advances in Neural Information Processing Systems*, 36:28541–28564, 2023. [2](#)
- [17] Weixiong Lin, Ziheng Zhao, Xiaoman Zhang, Chaoyi Wu, Ya Zhang, Yanfeng Wang, and Weidi Xie. Pmc-clip: Contrastive language-image pre-training using biomedical documents. In *International Conference on Medical Image Computing and Computer-Assisted Intervention*, pages 525–536. Springer, 2023. [1](#), [2](#), [3](#), [5](#), [6](#), [8](#)
- [18] Shilong Liu, Feng Li, Hao Zhang, Xiao Yang, Xianbiao Qi, Hang Su, Jun Zhu, and Lei Zhang. DAB-DETR: Dynamic anchor boxes are better queries for DETR. In *International Conference on Learning Representations*, 2022. [3](#)

[19] Xinyu Liu, Wuyang Li, and Yixuan Yuan. Diffrect: Latent diffusion label rectification for semi-supervised medical image segmentation. In *International Conference on Medical Image Computing and Computer-Assisted Intervention*, pages 56–66. Springer, 2024. 6

[20] Alejandro Lozano, Min Woo Sun, James Burgess, Liangyu Chen, Jeffrey J Nirschl, Jeffrey Gu, Ivan Lopez, Josiah Akililu, Austin Wolfgang Katzer, Collin Chiu, et al. Biomedica: An open biomedical image-caption archive, dataset, and vision-language models derived from scientific literature. *arXiv preprint arXiv:2501.07171*, 2025. 1, 2, 3, 5, 8

[21] Nitesh Methani, Pritha Ganguly, Mitesh M. Khapra, and Pratyush Kumar. Plotqa: Reasoning over scientific plots. In *The IEEE Winter Conference on Applications of Computer Vision (WACV)*, 2020. 3

[22] Norman Mu, Alexander Kirillov, David Wagner, and Saining Xie. Slip: Self-supervision meets language-image pre-training. In *European conference on computer vision*, pages 529–544. Springer, 2022. 2

[23] Andre GC Pacheco, Gustavo R Lima, Amanda S Salomao, Breno Krohling, Igor P Biral, Gabriel G de Angelo, Fábio CR Alves Jr, José GM Esgario, Alana C Simora, Pedro BC Castro, et al. Pad-ufes-20: A skin lesion dataset composed of patient data and clinical images collected from smartphones. *Data in brief*, 32:106221, 2020. 3

[24] Obioma Pelka, Sven Koitka, Johannes Rückert, Felix Nensa, and Christoph M Friedrich. Radiology objects in context (roco): a multimodal image dataset. In *Intravascular Imaging and Computer Assisted Stenting and Large-Scale Annotation of Biomedical Data and Expert Label Synthesis: 7th Joint International Workshop, CVII-STENT 2018 and Third International Workshop, LABELS 2018, Held in Conjunction with MICCAI 2018, Granada, Spain, September 16, 2018, Proceedings 3*, pages 180–189. Springer, 2018. 1, 2, 3, 8

[25] Fabiola Quintero-Rivera, Qiongchao J. Xi, Kim M. Keppeler-Noreuil, Ji Hyun Lee, Anne W. Higgins, Raymond M. Ancham, Amy E. Roberts, Ihn Sik Seong, Xueping Fan, Kasper Lage, Lily Y. Lu, Joanna Tao, Xuchen Hu, Ronald Berezney, Bruce D. Gelb, Anna Kamp, Ivan P. Moskowitz, Ronald V. Lacro, Weining Lu, Cynthia C. Morton, James F. Gusella, and Richard L. Maas. Matr3 disruption in human and mouse associated with bicuspid aortic valve, aortic coarctation and patent ductus arteriosus. *Human Molecular Genetics*, 24(8):2375–2389, 2015. 1

[26] Qwen, :, An Yang, Baosong Yang, Beichen Zhang, Binyuan Hui, Bo Zheng, Bowen Yu, Chengyuan Li, Dayiheng Liu, Fei Huang, Haoran Wei, Huan Lin, Jian Yang, Jianhong Tu, Jianwei Zhang, Jianxin Yang, Jiaxi Yang, Jingren Zhou, Junyang Lin, Kai Dang, Keming Lu, Keqin Bao, Kexin Yang, Le Yu, Mei Li, Mingfeng Xue, Pei Zhang, Qin Zhu, Rui Men, Runji Lin, Tianhao Li, Tianyi Tang, Tingyu Xia, Xingzhang Ren, Xuancheng Ren, Yang Fan, Yang Su, Yichang Zhang, Yu Wan, Yuqiong Liu, Zeyu Cui, Zhenru Zhang, and Zihan Qiu. Qwen2.5 technical report, 2025. 2, 5

[27] Alec Radford, Jong Wook Kim, Chris Hallacy, Aditya Ramesh, Gabriel Goh, Sandhini Agarwal, Girish Sastry, Amanda Askell, Pamela Mishkin, Jack Clark, et al. Learning transferable visual models from natural language supervision. In *International conference on machine learning*, pages 8748–8763. PMLR, 2021. 1, 2

[28] Khaled Saab, Tao Tu, Wei-Hung Weng, Ryutaro Tanno, David Stutz, Ellery Wulczyn, Fan Zhang, Tim Strother, Chunjong Park, Elahe Vedadi, Juanma Zambrano Chaves, Szu-Yeu Hu, Mike Schaeckermann, Aishwarya Kamath, Yong Cheng, David G. T. Barrett, Cathy Cheung, Basil Mustafa, Anil Palepu, Daniel McDuff, Le Hou, Tomer Golany, Luyang Liu, Jean baptiste Alayrac, Neil Houldsby, Nenad Tomasev, Jan Freyberg, Charles Lau, Jonas Kemp, Jeremy Lai, Shekoofeh Azizi, Kimberly Kanada, SiWai Man, Kavita Kulkarni, Ruoxi Sun, Siamak Shakeri, Luheng He, Ben Caine, Albert Webson, Natasha Latysheva, Melvin Johnson, Philip Mansfield, Jian Lu, Ehud Rivlin, Jesper Anderson, Bradley Green, Renee Wong, Jonathan Krause, Jonathon Shlens, Ewa Dominowska, S. M. Ali Eslami, Katherine Chou, Claire Cui, Oriol Vinyals, Koray Kavukcuoglu, James Manyika, Jeff Dean, Demis Hassabis, Yossi Matias, Dale Webster, Joelle Barral, Greg Corrado, Christopher Semturs, S. Sara Mahdavi, Juraj Gottweis, Alan Karthikesalingam, and Vivek Natarajan. Capabilities of gemini models in medicine, 2024. 2

[29] Christoph Schuhmann, Richard Vencu, Romain Beaumont, Robert Kaczmarczyk, Clayton Mullis, Aarush Katta, Theo Coombes, Jenia Jitsev, and Aran Komatsuzaki. Laion-400m: Open dataset of clip-filtered 400 million image-text pairs. *arXiv preprint arXiv:2111.02114*, 2021. 2

[30] Christoph Schuhmann, Romain Beaumont, Richard Vencu, Cade Gordon, Ross Wightman, Mehdi Cherti, Theo Coombes, Aarush Katta, Clayton Mullis, Mitchell Wortsman, et al. Laion-5b: An open large-scale dataset for training next generation image-text models. *Advances in Neural Information Processing Systems*, 35:25278–25294, 2022. 2

[31] Sanjay Subramanian, Lucy Lu Wang, Sachin Mehta, Ben Bogin, Madeleine van Zuylen, Sravanthi Parasa, Sameer Singh, Matt Gardner, and Hannaneh Hajishirzi. Medicat: A dataset of medical images, captions, and textual references. *arXiv preprint arXiv:2010.06000*, 2020. 3, 8

[32] Rich Sutton. The bitter lesson. 2019. 2

[33] Philipp Tschandl, Cliff Rosendahl, and Harald Kittler. The ham10000 dataset, a large collection of multi-source dermatoscopic images of common pigmented skin lesions. *Scientific data*, 5(1):1–9, 2018. 3

[34] Satoshi Tsutsui and David J Crandall. A data driven approach for compound figure separation using convolutional neural networks. In *2017 14th IAPR International Conference on Document Analysis and Recognition (ICDAR)*, pages 533–540. IEEE, 2017. 8

[35] Aaron van den Oord, Yazhe Li, and Oriol Vinyals. Representation learning with contrastive predictive coding. *arXiv preprint arXiv:1807.03748*, 2018. 2, 5, 1

[36] Frank Wilcoxon. Individual comparisons by ranking methods. *Biometrics Bulletin*, 1(6):80–83, 1945. 6

[37] Hu Xu, Saining Xie, Xiaoqing Ellen Tan, Po-Yao Huang, Russell Howes, Vasu Sharma, Shang-Wen Li, Gargi Ghosh, Luke Zettlemoyer, and Christoph Feichtenhofer. Demystifying clip data, 2024. 2

[38] Jiancheng Yang, Rui Shi, and Bingbing Ni. Medmnist classification decathlon: A lightweight automl benchmark for medical image analysis. In *IEEE 18th International Symposium on Biomedical Imaging (ISBI)*, pages 191–195, 2021. 3

[39] Jiancheng Yang, Rui Shi, Donglai Wei, Zequan Liu, Lin Zhao, Bilian Ke, Hanspeter Pfister, and Bingbing Ni. Medmnist v2-a large-scale lightweight benchmark for 2d and 3d biomedical image classification. *Scientific Data*, 10(1):41, 2023. 3

[40] Lewei Yao, Runhui Huang, Lu Hou, Guansong Lu, Minzhe Niu, Hang Xu, Xiaodan Liang, Zhenguo Li, Xin Jiang, and Chunjing Xu. Filip: Fine-grained interactive language-image pre-training. *arXiv preprint arXiv:2111.07783*, 2021. 2

[41] Tianyuan Yao, Chang Qu, Quan Liu, Ruining Deng, Yuanhan Tian, Jiachen Xu, Aadarsh Jha, Shunxing Bao, Mengyang Zhao, Agnes B Fogo, et al. Compound figure separation of biomedical images with side loss. In *Deep Generative Models, and Data Augmentation, Labelling, and Imperfections: First Workshop, DGM4MICCAI 2021, and First Workshop, DALI 2021, Held in Conjunction with MICCAI 2021, Strasbourg, France, October 1, 2021, Proceedings 1*, pages 173–183. Springer, 2021. 8

[42] Qingjie Zeng, Yutong Xie, Zilin Lu, and Yong Xia. Pefat: Boosting semi-supervised medical image classification via pseudo-loss estimation and feature adversarial training. In *Proceedings of the IEEE/CVF conference on computer vision and pattern recognition*, pages 15671–15680, 2023. 6

[43] Sheng Zhang, Yanbo Xu, Naoto Usuyama, Hanwen Xu, Jaspreet Bagga, Robert Tinn, Sam Preston, Rajesh Rao, Mu Wei, Naveen Valluri, et al. Biomedclip: a multimodal biomedical foundation model pretrained from fifteen million scientific image-text pairs. *arXiv preprint arXiv:2303.00915*, 2023. 1, 2, 5, 6, 8

[44] Ángel E. Esteban, Miguel López-Pérez, Adrián Colomer, María A. Sales, Rafael Molina, and Valery Naranjo. A new optical density granulometry-based descriptor for the classification of prostate histological images using shallow and deep gaussian processes. *Computer Methods and Programs in Biomedicine*, 178:303–317, 2019. 3

Open-PMC-18M: A High-Fidelity Large Scale Medical Dataset for Multimodal Representation Learning

Supplementary Material

A. Additional Dataset Statistics

We provide additional dataset statistics in visualizations in this section (see Figure 4).

B. Training Details

B.1. Encoder Pretraining

As a first step, we train separate encoders for image and text modalities by aligning their representations using a vanilla contrastive loss. Let φ denote an image encoder and ψ denote a text encoder that maps images and text to a common representation space, respectively. Given a batch of training samples $B = \{(x_i, t_i)\}_{i=1}^N$, where x_i and t_i denote the i^{th} image and text instances respectively, the InfoNCE loss [35] is optimized by minimizing the distance between the representations of an image and its corresponding text, $(\varphi(x_i), \psi(t_i))$, while maximizing the distance between unrelated image-text representation pairs, $(\varphi(x_i), \psi(t_j))$, $i \neq j$:

$$\ell_{\text{con}}(x_i, t_i; B) = - \left(\log \frac{\exp(\langle \varphi(x_i), \psi(t_i) \rangle / \tau)}{\sum_{k=1}^N \exp(\langle \varphi(x_i), \psi(t_k) \rangle / \tau)} + \log \frac{\exp(\langle \varphi(x_i), \psi(t_i) \rangle / \tau)}{\sum_{k=1}^N \exp(\langle \varphi(x_k), \psi(t_i) \rangle / \tau)} \right) \quad (1)$$

where $\langle \cdot, \cdot \rangle$ denotes similarity between two vectors (e.g. cosine similarity), and $\tau > 0$ is a temperature parameter. For simplicity of notation, we drop B and denote the loss for (x, t) by $\ell_{\text{con}}(x, t)$. Multimodal contrastive learning trains encoders φ and ψ by minimizing Eq. 1 over the pairs in B :

$$\ell_{\text{multimodal}} = \min_{\varphi, \psi} \mathbb{E}_B \left[\frac{1}{N} \sum_{i=1}^N \ell_{\text{con}}(x_i, t_i) \right]. \quad (2)$$

B.2. Training Hyperparameters

For pretraining, we use the AdamW optimizer with a weight decay of 0.2, $\beta_1 = 0.9$, and $\beta_2 = 0.98$. The learning rate is scheduled using cosine decay, with a linear warmup over the first 10% of the total training steps. We apply gradient accumulation with a frequency of 4. Training is performed on 8 NVIDIA A100 GPUs with a total batch size of 2048. The initial learning rate is set to 5.0×10^{-4} , and models are trained for 64 epochs.

B.3. Performance on Validation set

We use a 50,000-sample subset of the dataset as our validation set. Each sample includes a sub-figure and its paired sub-caption. Retrieval is used as the validation task, and $\text{recall}@200$ is the metric for selecting the best epoch. Figure 5 presents the $\text{recall}@200$ scores for the final epochs of training. The results show a rising trend that eventually levels off, indicating stable validation performance.

C. Evaluation Datasets

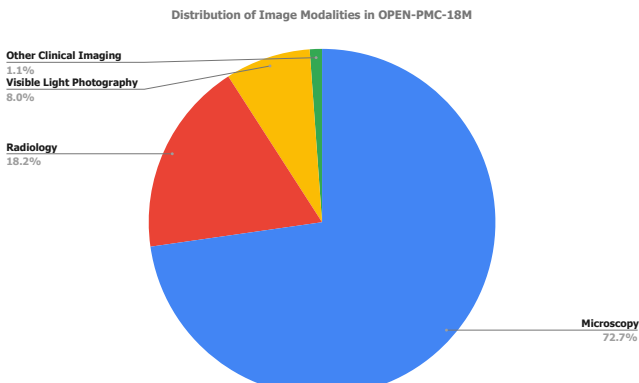
We evaluate our pretrained models on three downstream tasks: image-text retrieval, zero-shot classification, and linear probing. A summary of the evaluation datasets used for these tasks is provided in Table 5.

MIMIC-CXR: MIMIC-CXR contains 377,110 de-identified chest X-ray images from 65,379 patients, accompanied by free-text reports. The dataset was collected from the emergency department of Beth Israel Deaconess Medical Center. Each patient typically has multiple views and a corresponding radiology report labeled using the CheXpert labeling tool (Irvin et al., 2019), which identifies 13 common conditions such as atelectasis, cardiomegaly, consolidation, pleural effusion, and pneumonia.

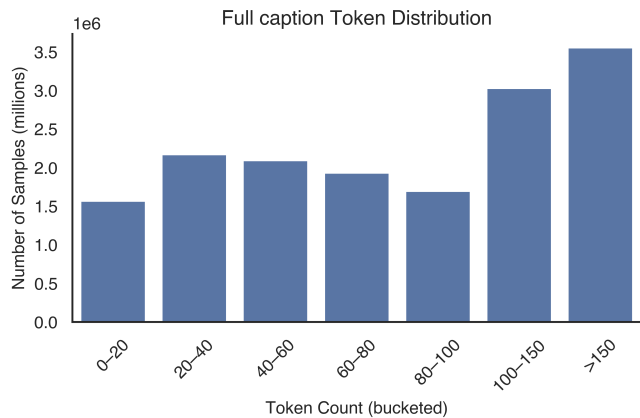
Quilt-1M: Quilt-1M comprises over one million histopathology image-text pairs. The largest subset, Quilt, includes 802,144 pairs extracted from 1,087 hours of educational histopathology videos on YouTube. Captions were generated using a combination of large language models, handcrafted rules, and automatic speech recognition. Additional subsets come from PubMed Open Access, LAION-5B, and OpenPath Twitter data, resulting in a combined dataset of over one million pairs.

DeepEyeNet: DeepEyeNet is a large-scale retinal image dataset comprising 15,709 images, including both color fundus photography (CFP) and fluorescein angiography (FA). Each image is annotated with three expert-defined labels: a disease or symptom name, a set of relevant keywords, and a detailed clinical description. The dataset covers 265 distinct retinal conditions.

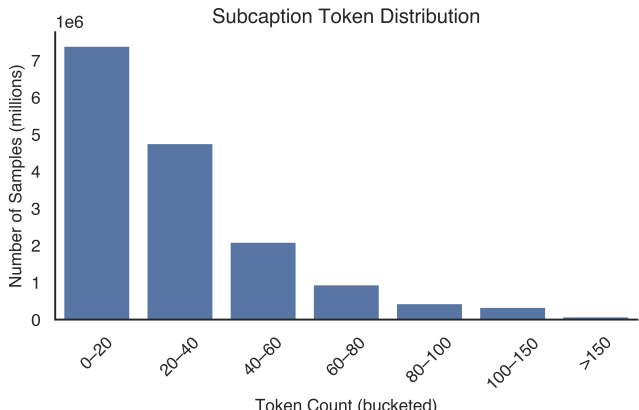
SICAP: The Prostate Cancer Grade Assessment (SICAP) dataset comprises prostate histology whole-slide images an-



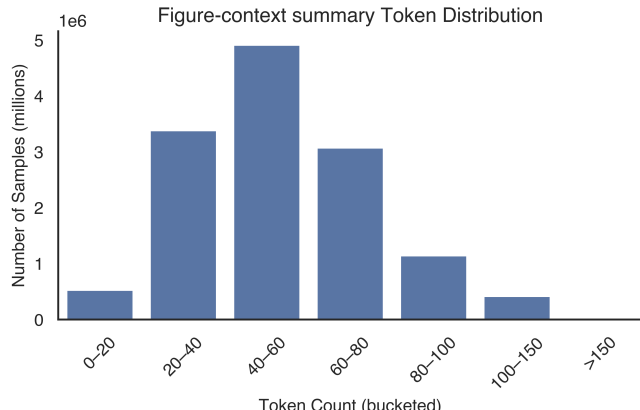
(a) Distribution of image modalities in OPEN-PMC-18M.



(b) Full caption token distribution.



(c) Subcaption token distribution.



(d) Figure-context summary token distribution.

Figure 4. Dataset composition and text length statistics. (a) Distribution of image modalities in OPEN-PMC-18M. (b) Token distribution for full captions. (c) Token distribution for subcaptions. (d) Token distribution for figure-context summaries.

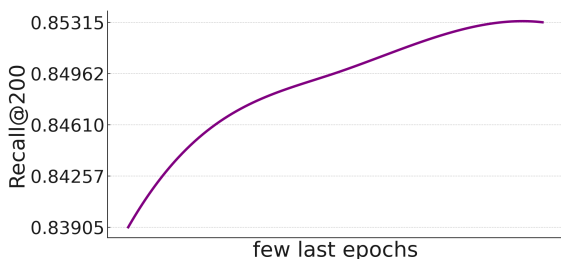


Figure 5. Recall@200 for the last epochs of the trained model on the validation data

notated with global Gleason scores and path-level Gleason grades, supporting research in automated prostate cancer grading.

PAD-UFES-20: PAD-UFES-20 includes 2,298 clinical images of six types of skin lesions, each accompanied by up to 22 patient metadata features, facilitating studies in skin lesion classification.

Skin Cancer: This dataset contains 2,357 dermatoscopic images of skin lesions, labeled with diagnostic categories, aiding in the development of skin cancer detection models.

PCam (PatchCamelyon): PCam consists of 327,680 color images (96×96 px) extracted from histopathologic scans of lymph node sections, each labeled to indicate the presence of metastatic tissue.

NCT-CRC-HE: The NCT-CRC-HE dataset comprises 100,000 non-overlapping image patches from H&E-stained histological images of human colorectal cancer and normal tissue, supporting research in histopathological image analysis.

LC-Lung: LC-Lung includes 15,000 histopathological images of lung tissue, categorized into benign and malignant classes, useful for lung cancer classification studies.

Table 5. Evaluation datasets.

Task	Setup	Dataset	Modality	Nb. Samples
Retrieval	I→T & T→I	Quilt-1M	Histopathology	13,559
		MIMIC-IV-CXR	Chest X-ray	3,269
		DeepEyeNet	Retina	3,140
Zero-shot classification & Linear probing	6 classes	PAD-UFES-20	Dermatology	460
	7 classes	SkinCancer	Dermatology	2,003
	2 classes	PatchCamelyon (PCam)	Histopathology	32,768
	8 classes	NCT-CRC-HE-100K	Histopathology	6,333
	3 classes	LC25000Lung	Histopathology	3,000
	2 classes	LC25000Colon	Histopathology	2,000
	4 classes	BACH	Histopathology	100
	4 classes	SICAPv2	Histopathology	2,122
	9 classes	PathMNIST+	Colon Pathology	107,180
	7 classes	DermaMNIST+	Dermatoscope	10,015
	4 classes	OctMNIST+	Retinal OCT	109,309
	2 classes	PneumoniaMNIST+	Chest X-Ray	5,856
	5 classes	RetinaMNIST+	Fundus Camera	1,600
	2 classes	BreastMNIST+	Breast Ultrasound	780
	8 classes	BloodMNIST+	Blood Cell Microscope	17,092
	8 classes	TissueMNIST+	Kidney Cortex Microscope	236,386
	11 classes	OrganAMNIST+	Abdominal CT	58,830
	11 classes	OrganCMNIST+	Abdominal CT	23,583
	11 classes	OrganSMNIST+	Abdominal CT	25,211

LC-Colon: LC-Colon comprises 10,000 histopathological images of colon tissue, labeled as benign or malignant, aiding in colon cancer detection research.

BACH: The Breast Cancer Histology (BACH) dataset contains microscopy images of breast tissue, annotated across four classes: normal, benign, in situ carcinoma, and invasive carcinoma, facilitating automated breast cancer diagnosis.

DermaMNIST+: DermaMNIST+ consists of 10,015 dermatoscopic images categorized into seven skin disease classes, serving as a benchmark for skin lesion classification tasks.

OCTMNIST+: OCTMNIST+ includes 109,309 optical coherence tomography images labeled for retinal diseases like choroidal neovascularization, diabetic macular edema, and drusen, supporting ophthalmic image classification.

PneumoniaMNIST+: PneumoniaMNIST+ is based on 5,856 pediatric chest X-ray images, labeled for pneumonia detection, aiding in the development of automated pneumonia diagnosis models.

RetinaMNIST+: RetinaMNIST+ comprises 1,600 retinal fundus images labeled for common eye diseases, useful for training models in automated retinal disease classification.

BreastMNIST+: BreastMNIST+ contains 780 ultrasound images of breast tumors, labeled as benign or malignant, supporting breast cancer detection research.

BloodMNIST+: BloodMNIST+ consists of 17,092 microscopic images of blood cells, classified into eight cell types, facilitating automated classification tasks in hematology.

TissueMNIST+: TissueMNIST+ includes 236,386 microscopic images of tissue samples from different organs,

labeled according to tissue type, supporting histopathological analysis.

PathMNIST+: PathMNIST+ is derived from colorectal cancer tissue slides, containing 107,180 images labeled with nine different tissue classes, aiding in multi-class classification tasks in pathology.

OrganAMNIST+: OrganAMNIST+ consists of 58,850 abdominal CT images labeled with different anatomical organ classes, supporting organ segmentation and classification tasks.

OrganCMNIST+: OrganCMNIST+ contains 23,600 coronal CT images of various organs, labeled for organ classification tasks, used for research in medical image understanding.

OrganSMNIST+: OrganSMNIST+ comprises 23,600 sagittal CT images of multiple organs, annotated for classification, aiding in comprehensive medical imaging analysis.

C.1. Representations Analysis

To explore differences in the structure of learned image representations, we project the embedding spaces of three benchmark sets, each constructed by combining datasets used for retrieval and zero-shot classification across radiology, microscopy, and visible light photography (VLP), into two dimensions using t-SNE (Figure 6). The radiology benchmark includes MIMIC-CXR and other related zero-shot classification tasks, totaling approximately 41,000 samples. The microscopy and VLP benchmarks contain approximately 20,000 and 6,000 samples, respectively. To quantify differences between the embedding distributions, we compute the Maximum Mean Discrepancy (MMD) [9]. Given a dataset X (e.g., all radiology samples), we extract embeddings $\phi(X)$ and $\psi(X)$ using vision encoders ϕ and ψ trained on OPEN-PMC-18M and PMC-6M, respectively. To assess whether the differences between these distributions are statistically significant, we perform a permutation test by randomly reassigning samples and recomputing MMD over 100 iterations to generate an empirical null distribution.

Visual inspection of the embeddings reveals distinct representational structures between the two models. This distinction is particularly evident in microscopy and VLP, where the latent spaces of the two models are more clearly differentiated. In contrast, radiology embeddings appear more intermixed, with less visual separation between the models' representation spaces. Nonetheless, the MMD analysis confirms that the observed differences are statistically significant across all modalities. For the aggregated radiology dataset, the observed MMD is 0.0214 (null

range: 0.0186–0.0214; $p = 0.005$). For the aggregated microscopy dataset, the observed MMD is 0.0212 (null range: 0.0188–0.0212; $p < 0.001$). For the VLP dataset, the observed MMD is again 0.0214 (null range: 0.0186–0.0214; $p = 0.007$). These results indicate that models trained on subfigure-level data yield significantly different representation spaces compared to those trained on compound figures.

D. Prompts

We present our subcaption extraction, summary generation and subcaption extraction evaluation judge prompt in this section. Figure 7 illustrates the prompt used for subcaption extraction with the Qwen2.5-VL-32B-Instruct model. Figure 8 presents the prompt for summary generation using the Qwen2.5-14B-Instruct model.

E. Additional Subfigure Extraction Results

Figure 9 showcases examples from the ImageCLEF 2016 dataset and from a subset of PMC-6M, illustrating accurate detection of distinct subfigures across diverse panel layouts and content types.

F. Evaluation Results

F.1. Retrieval

In addition to the results of recall at 200 which was included in the main body of the paper, we also provide the results for recall at 10 (Table 6) and recall at 50 (Table 7).

F.2. Zeroshot Classification

To assess the strength of the learned representations, we evaluate each model in a zero-shot classification setting. We use the model's frozen image and text encoders without any task-specific training. Classification is done by comparing image features with the text prompts of each class and selecting the class with the highest similarity score. The results of the zero-shot experiments are shown in Table 8.

F.3. Linear Probing

To evaluate the quality of the learned image representations, we perform linear probing using a single-layer MLP on the downstream task datasets. Each model is trained for 40 epochs with a cosine annealing learning rate schedule, starting from an initial learning rate of 0.1. The results are presented in Table 9.

Table 6. Retrieval performance (Recall@10) of all models trained on paired image-caption pairs in the medical domain. The last column, Average Recall (AR), aggregates the results across all tasks.

Model	Image-to-Text			Text-to-Image			AR
	MIMIC	Quilt	DeepEyeNet	MIMIC	Quilt	DeepEyeNet	
PMC-OA	0.014	0.020	0.026	0.010	0.016	0.017	0.017
OPEN-PMC	0.022	0.018	0.024	0.016	0.016	0.024	0.020
BioMedCLIP	0.022	0.024	0.031	0.015	0.027	0.024	0.023
BIOMEDICA	0.005	0.033	0.023	0.006	0.041	0.022	0.021
PMC-6M	0.033	0.028	0.039	0.028	0.032	0.035	0.032
OPEN-PMC-18M	0.023	0.033	0.033	0.019	0.039	0.041	0.031

Table 7. Retrieval performance (Recall@50) of all models trained on paired image-caption pairs in the medical domain. The last column, Average Recall (AR), aggregates the results across all tasks.

Model	Image-to-Text			Text-to-Image			AR
	MIMIC	Quilt	DeepEyeNet	MIMIC	Quilt	DeepEyeNet	
PMC-OA	0.054	0.062	0.071	0.044	0.056	0.070	0.059
OPEN-PMC	0.072	0.059	0.058	0.056	0.053	0.077	0.062
BioMedCLIP	0.067	0.070	0.074	0.055	0.082	0.074	0.070
BIOMEDICA	0.024	0.084	0.071	0.030	0.102	0.067	0.63
PMC-6M	0.106	0.087	0.092	0.097	0.098	0.088	0.094
OPEN-PMC-18M	0.078	0.105	0.090	0.072	0.113	0.105	0.093

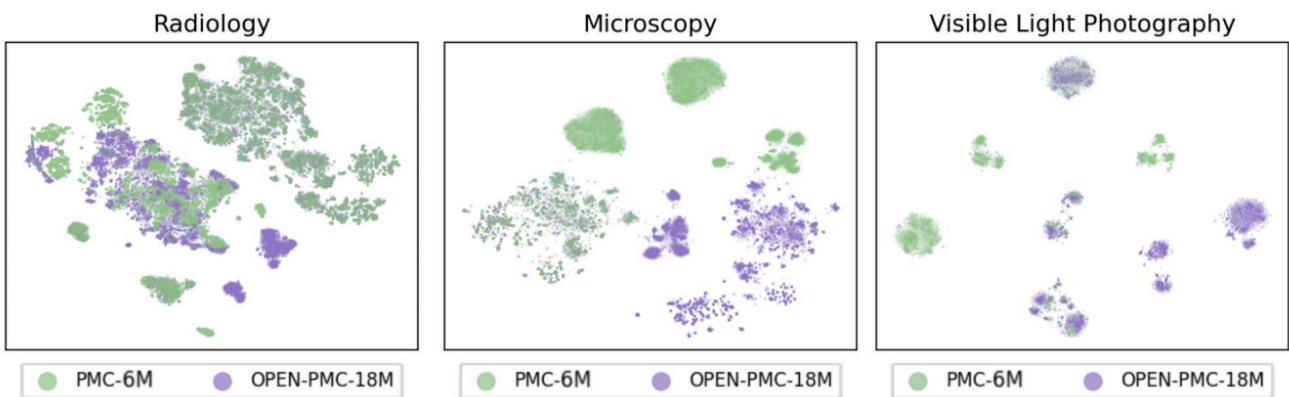


Figure 6. t-SNE visualizations of models embeddings trained on OPEN-PMC-18M and PMC-6M on three imaging modalities, illustrating the structure and separation of the learned representation spaces. MMD analysis reveals statistically significant differences in embedding distributions across all imaging modalities.

Prompt: Subcaption extraction

INSTRUCTIONS:

You are an expert medical image image captioning assistant. Your task is the following:

1. You will be provided with a subfigure image that is part of a full image figure and the full figure caption in the input.
2. The full caption contains descriptions for multiple subfigures (e.g., Subfigure-A, Subfigure-B, etc.).
3. Your task is to identify the relevant subfigure caption corresponding to the provided subfigure image from the full caption exactly as it appears.
4. If the subcaption is written jointly for two or more subfigures (e.g., A-C together, (A-C), Axial (A) and coronal (B), etc.), copy that combined description exactly as it appears.
5. Do NOT rewrite, summarize, or generate new text. Copy the relevant portion exactly as it appears in the full caption.
6. Here, "exactly as it appears" means the extracted caption must match word-for-word, character-for-character with the correct subfigure caption text from the full caption. It must be a verbatim copy, not paraphrased, summarized, or partially copied.
7. If no relevant caption is found in the full caption, output the verbatim copy of the entire full caption.

OUTPUT FORMAT:

```
<caption><EXTRACTED SUBFIGURE CAPTION OR VERBATIM FULL CAPTION></caption>
```

Figure 7. An example prompt used for subcaption extraction with the Qwen2.5-VL-32B-Instruct model.

Prompt: Figure-context summary generation

INSTRUCTIONS:

You will be provided with:

1. A subcaption that describes a subfigure from a compound figure.
2. The full caption of the compound figure.
3. A context passage related to the compound figure.

Definition of compound figure: A compound figure is a figure that contains multiple subfigures of the same topic (e.g., panels A, B, C, etc.).

Your task is to summarize only the portions of the context passage that are most relevant to the given subcaption. The full caption is provided for additional information.

The summary should:

- Use both the subcaption and the full caption to determine context.
- Be concise and focused on the subcaption's content.
- Exclude unrelated information from the context passage.
- Preserve key biomedical terminology exactly as it appears.
- Output the summary only, without any labels or additional text in the following format:

```
<summary>  
<YOUR SUMMARY OF THE CONTEXT PASSAGE RELEVANT TO THE SUBCAPTION AND FULL  
CAPTION>  
</summary>
```

Figure 8. An example prompt for figure-context summary generation using the Qwen2.5-14B-Instruct model.

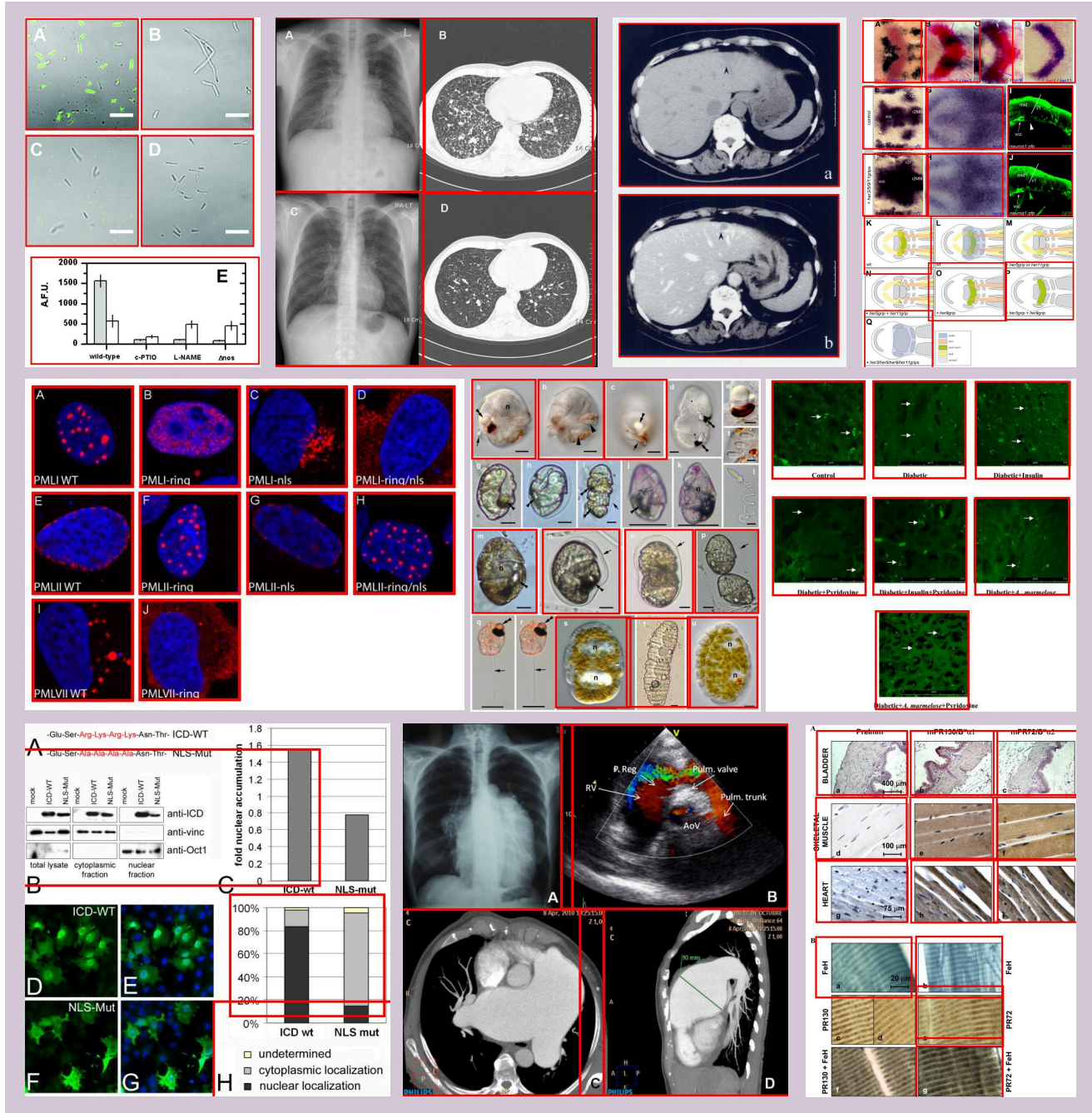


Figure 9. Qualitative examples of subfigure detection using our DAB-DETR model. Shown are real-world biomedical compound figures from ImageCLEF 2016. Our model accurately localizes and separates distinct subfigures, even in heterogeneous, densely packed, or non-uniform layouts.

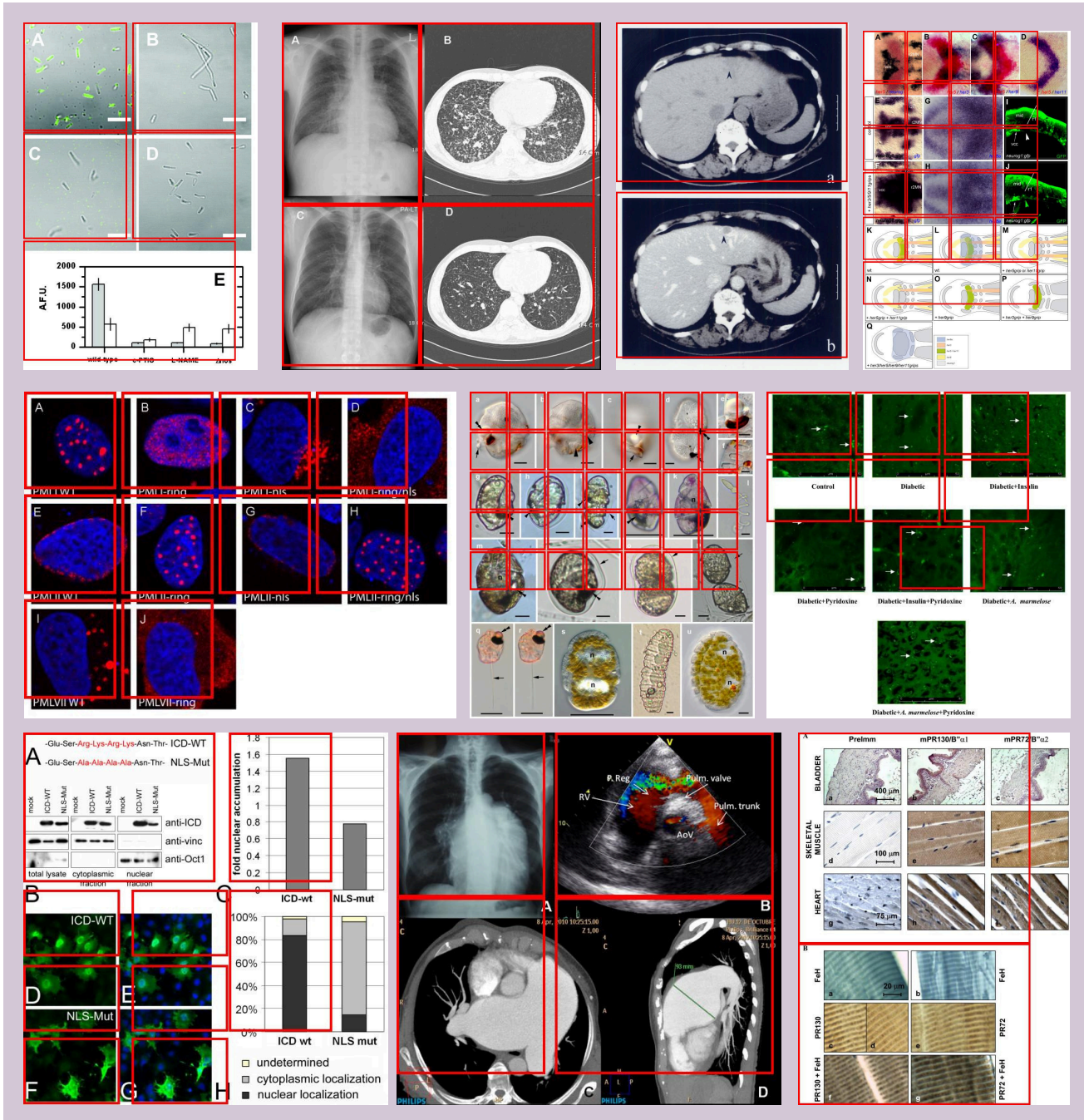


Figure 10. Qualitative results of subfigure detection using Qwen2.5-VL-32B-Instruct on the same examples in Figure 9 from ImageCLEF 2016. While Qwen can identify some coarse panel structure, it frequently under-segments, over-segments, or fails to localize several subfigures, especially in heterogeneous or irregular layouts, highlighting the advantages of our DAB-DETR model.

Table 8. Zero-shot classification F1-scores across diverse medical datasets for different models. Highest performance values are in bold, second-best are underlined.

Model	Radiology						Average		
	PneumoniaMNIST+	BreastMNIST+	OrganAMNIST+	OrganCMNIST+	OrganSMNIST+				
PMC-OA	50.94	52.36	19.70	14.79	16.99	30.95			
OPEN-PMC	50.13	59.65	27.95	23.23	20.03	36.19			
BioMedCLIP	60.13	33.76	19.40	14.12	16.00	28.62			
BIOMEDICA	38.46	56.66	19.25	17.13	16.33	29.56			
PMC-6M	68.81	26.87	23.48	14.68	17.57	30.28			
OPEN-PMC-18M	38.46	61.18	28.43	24.28	20.38	<u>34.55</u>			
Model	Visible Light Photography						Average		
	PAD-UFES-20	Skin Cancer	PathMNIST+	DermaMNIST+	OCTMNIST+	RetinaMNIST+			
PMC-OA	17.18	13.30	56.03	14.29	50.74	27.22	29.79		
OPEN-PMC	21.11	13.56	49.16	14.60	45.27	26.12	28.30		
BioMedCLIP	24.41	13.62	42.27	14.07	11.87	20.82	21.17		
BIOMEDICA	40.57	17.20	49.10	21.89	10.00	18.53	26.21		
PMC-6M	33.04	16.56	52.17	17.52	46.91	22.81	<u>31.50</u>		
OPEN-PMC-18M	27.00	17.64	66.02	14.16	37.71	30.09	32.10		
Model	Microscopy						Average		
	Sicap	PCam	NCT-CRC-HE	LC-Lung	LC-Colon	BACH	BloodMNIST+	TissueMNIST+	
PMC-OA	32.80	70.65	43.95	56.04	91.05	33.75	5.57	7.17	42.62
OPEN-PMC	20.71	38.96	42.88	63.97	88.38	41.31	10.73	6.08	39.12
BIOMEDICA	31.80	62.17	48.98	70.93	84.43	39.83	4.37	4.31	43.35
BioMedCLIP	41.53	72.57	49.46	76.63	86.54	23.88	6.83	3.86	45.16
PMC-6M	22.89	68.05	55.28	86.86	78.41	52.58	3.72	3.05	<u>46.35</u>
OPEN-PMC-18M	35.28	73.83	64.85	92.47	97.69	63.64	10.93	4.10	55.35

Table 9. Linear-probing F1-scores across diverse medical datasets for different models.

Radiology									
Model	PneumoniaMNIST+	BreastMNIST+	OrganAMNIST+	OrganCMNIST+	OrganSMNIST+	Average			
BioMedCLIP	92.96	75.63	85.71	79.29	64.88	79.69			
BIOMEDICA	86.15	77.16	89.72	82.66	70.93	81.12			
PMC-6M	79.74	77.84	89.56	85.00	69.07	80.24			
OPEN-PMC-18M	79.74	77.84	89.51	85.00	69.07	80.23			
Visible Light Photography									
Model	PAD-UFES-20	Skin Cancer	PathMNIST+	DermaMNIST+	OCTMNIST+	RetinaMNIST+	Average		
BioMedCLIP	62.31	56.43	90.27	59.62	71.70	42.95	63.88		
BIOMEDICA	82.59	68.09	88.32	74.02	80.17	52.11	74.21		
PMC-6M	75.62	61.61	91.28	61.47	80.17	46.10	69.37		
OPEN-PMC-18M	75.62	62.92	91.35	61.47	78.73	46.59	69.44		
Microscopy									
Model	Sicap	PCam	NCT-CRC-HE	LC-Lung	LC-Colon	BACH	BloodMNIST+	TissueMNIST+	Average
BioMedCLIP	63.84	83.00	72.56	96.83	99.75	73.01	95.43	43.71	78.51
BIOMEDICA	65.15	86.41	83.57	99.26	99.95	75.65	96.92	50.69	82.2
PMC-6M	60.00	84.22	64.64	98.85	99.80	62.39	95.87	49.89	76.95
OPEN-PMC-18M	59.85	84.16	64.64	98.85	99.80	65.52	95.87	49.96	77.33